The neural circuit mechanism for auditory responses in the mediodorsal thalamic nucleus of awake mice

Check for updates

Shuai Wang [1,4], Zijie Li[2,4], Bingqing Qiao[2], Shihui Kuai[1], Shiyue Fan[1], Ping Zhao[1] & Ling Qin [3]✉

The mediodorsal thalamic nucleus (MD) forms neural circuits with various brain regions, including the prefrontal cortex (PFC), the reticular thalamic nucleus (TRN), and the midbrain reticular nucleus (MRN). However, the specific roles and underlying mechanisms in auditory information processing remain unclear. Here, we perform multi-channel electrophysiological recordings in awake mice to investigate the response patterns of the MD to auditory stimuli, as well as the regulatory effects of PFC, MRN, and TRN inputs. We identify two distinct types of sound-evoked responses. The Phasic-response features a transient burst firing to the stimulus with short latency, rapidly adapting to baseline and corresponding to the onset fluctuation of the local field potential. The Sustained-response is marked by prolonged firing with longer latency and is accompanied by persistent enhancement of oscillatory power following stimulus offset. The response patterns of MD neurons remain consistent across different types of auditory stimuli. Optogenetic inactivation of the MRN suppresses both response types in the MD. The Sustained-response is attenuated by PFC inactivation but enhanced by TRN inactivation, while the Phasic-response remains unaffected by inactivation of either the PFC or TRN. Our findings expand the understanding of the MD's role in sound information integration and auditory cognitive regulation.

The mediodorsal thalamic nucleus (MD) is located in the medial part of the thalamus, between the internal medullary laminae and the periventricular gray matter. MD primarily consists of excitatory glutamatergic neurons[1,2]. As a higher-order thalamic nucleus, the MD forms extensive connections with various cortical regions and subcortical nuclei, contributing to a complex neural network involved in regulation of behavior and cognition. For instance, the MD receives inhibitory inputs from the reticular thalamic nucleus (TRN), which initiates and sustains spindle oscillations. These oscillations in the MD then synchronize with the prefrontal cortex (PFC) through the thalamo-cortical loop, contributing to memory consolidation during sleep[3,4]. The MD also receives inputs from the brainstem, transmitting them to the anterior cingulate cortex and motor cortex, where they participate in the selection, planning, and execution of goal-directed behaviors[5,6]. Additionally, the MD receives information from the basal ganglia and limbic system, playing a critical role in regulating emotional integration, reward processing, and cognitive flexibility[7–9]. Several pathologies have been associated with dysfunction of the MD. For instance, patients with schizophrenia exhibit reduced MD volume, which impairs working memory[3,10]. Patients with alcohol use disorder experience MD atrophy and decreased integrity of projections to the PFC, resulting in the impairments of motor control and planning ability[11,12]. Therefore, it is crucial to elucidate the physiological mechanisms of information processing within the neural network centered around the MD.

Previous studies have investigated the involvement of the MD in the transmission of olfactory and nociceptive information[8,13]. Recent studies have highlighted that the critical role of the MD in regulating auditory functions, such as sound detection sensitivity and auditory attention. Evidence suggests that the continuous interaction between the MD and the PFC regulates the balance between signal and noise, thereby optimizing auditory information processing in complex environment[14]. MD neurons are responsive to auditory stimuli and regulate behavioral flexibility when rodents perform choice-selection tasks[15]. Additionally, during auditory-guided conditioned reflex formation, the MD exhibits delayed neuronal activity following stimulation, suggesting its involvement in associating conditioned stimuli with rewards[16]. Our previous study also demonstrated robust auditory responses and gating effects in the MD[17]. Therefore, it is essential to elucidate the detailed characteristics and regulatory mechanisms underlying the auditory responses of the MD.

[1]Department of Anesthesiology, Shengjing Hospital of China Medical University, Shenyang, China. [2]Department of Physiology, School of Life Sciences, China Medical University, Shenyang, China. [3]Laboratory of Hearing Research, School of Life Sciences, China Medical University, Shenyang, China. [4]These authors contributed equally: Shuai Wang, Zijie Li. ✉e-mail: 20081029@cmu.edu.cn

As a critical hub of the thalamus, the MD receives both bottom-up inputs from glutamatergic neurons in the midbrain reticular nucleus (MRN)[5] and top-down control from the PFC[9,18]. In addition, within the intricate thalamic local network, the MD also receives GABAergic inhibitory inputs from the TRN[19,20]. Therefore, in investigating the auditory response characteristics and functional roles of the MD, it is essential to consider the integrative interactions between MD neuronal activity and input from its afferent regions, including the MRN, PFC, and TRN. We hypothesize that bottom-up input from the MRN may be responsible for triggering auditory responses in the MD, top-down input from the PFC to the MD may help sustain attention to auditory stimuli, and inhibitory input from the TRN may serve to gate the MD's capacity to process auditory information.

In this study, we applied multi-channel electrophysiological recordings and optogenetic manipulation to investigate the neural circuits underlying sound-evoked responses in the MD of awake mice. We identified two distinct response patterns: a Phasic-response characterized by transient burst firing and short latency, and a Sustained-response marked by prolonged firing and enhanced oscillatory power. These response patterns remained consistent despite variations in basic acoustic parameter. Optogenetic inhibition of the MRN attenuated both responses, while inhibition of the PFC primarily diminished the Sustained-response, and inhibition of the TRN enhanced it. Our findings, which reveal the sound-evoked response

patterns in MD neurons and their regulatory neural circuits, provide new insights into the MD's role in integrating sound information and regulating auditory cognition.

Results

The MD receives projections from the MRN, PFC and TRN

We initially employed a retrograde viral tracing approach to investigate the afferent connectivity of the MD by injecting Adeno-associated virus (AAV)-retro-hSyn-mCherry into the MD of C57BL/6 mice (Fig. 1A). Figure 1B displays the viral expression at the MD injection site. Quantitative analysis revealed a relatively high density of retrogradely labeled mCherry[+] cell in the TRN, PFC, and MRN (Fig. 1C, D), indicating these regions have relatively more direct neuronal projections to the MD. Immunofluorescence analysis confirmed that the majority of neurons in the MD are glutamatergic, as evidenced by Vglut2 staining, with a small proportion of GABAergic (Gad67^{+}) neurons (Fig. 1E–G).

Characteristics of sound-evoked response in MD neurons

To investigate the auditory response patterns of MD neurons in awake mice, we implanted a single-shank, 16-channel linear probe into the unilateral MD while presenting white noise stimuli (4-44 kHz, 80 ms duration, 50 dB intensity) to the contralateral side (Fig. 2A). Simultaneously, frontal
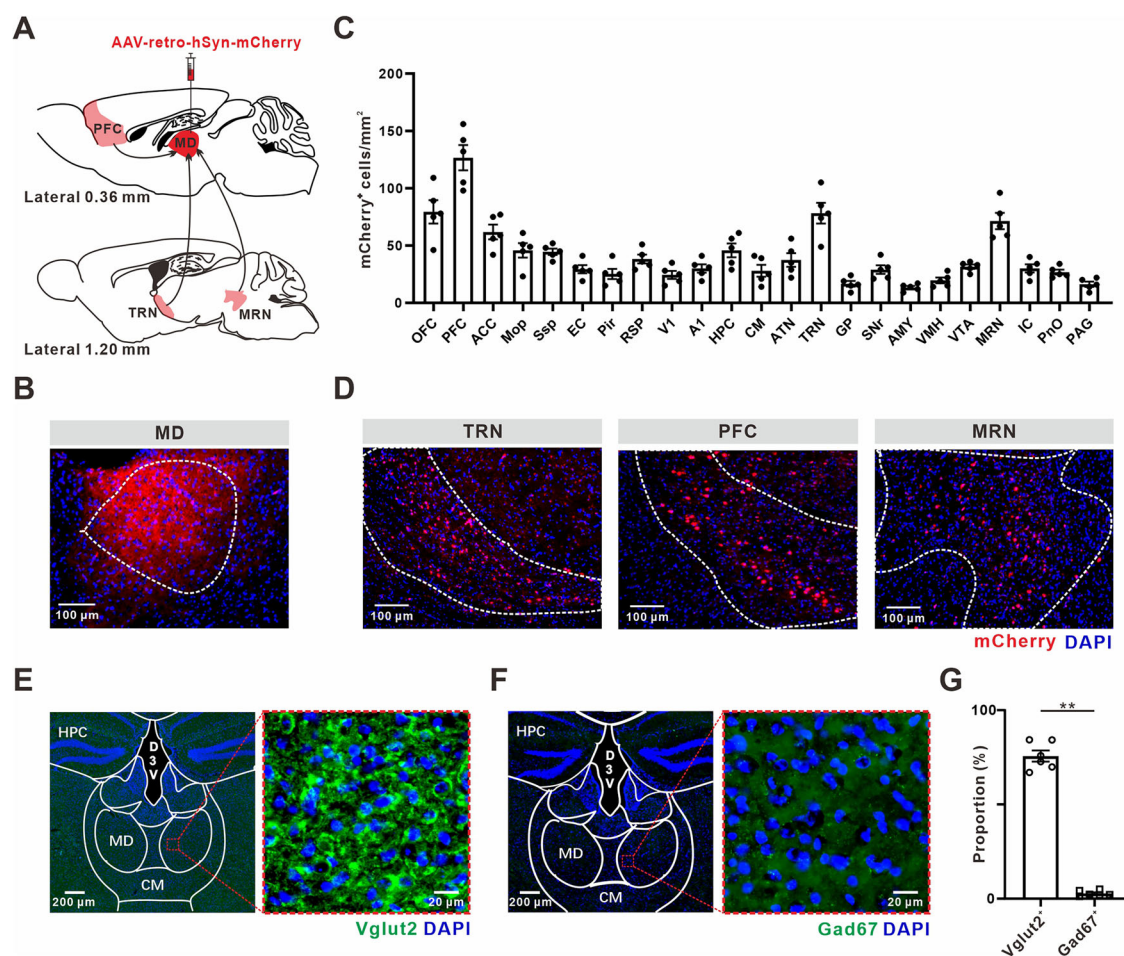

Fig. 1 | Projections of the MRN, PFC and TRN to the MD. A A schematic diagram of virus injections and retrograde tracing. Created by the authors. **B** Representative image of the injection site of AAV-retro-hSyn-mCherry in the MD. **C** Quantification of mCherry^{+} cells per mm² in various brain regions. Each point represents data from a single mouse. N = 5 mice. **D** Representative images of mCherry^{+} cells in the TRN, PFC, and MRN. **E** Immunofluorescence labeling showing Vglut2^{+} and DAPI staining in the MD. **F** Immunofluorescence labeling showing Gad67^{+} and DAPI staining in the MD. **G** Quantification of the proportion of Vglut2^{+} and Gad67^{+} cells in the MD. N = 6 mice per

group. [**]P < 0.01, Student's t tests. OFC orbitofrontal cortex, PFC prefrontal cortex, ACC anterior cingulate cortex, Mop primary motor cortex, Ssp primary somatosensory cortex, EC entorhinal cortex, Pir piriform cortex, RSP retrosplenial cortex, V1 primary visual cortex, A1 primary auditory cortex, HPC hippocampus, CM centromedian thalamic nucleus, ATN anterior thalamic nucleus, TRN reticular thalamic nucleus, GP globus pallidus, SNr substantia nigra pars reticulata, AMY amygdala, VMH ventromedial hypothalamus, VTA ventral tegmental area, MRN midbrain reticular nucleus, IC inferior colliculus, PnO pontine nucleus, PAG periaqueductal gray.
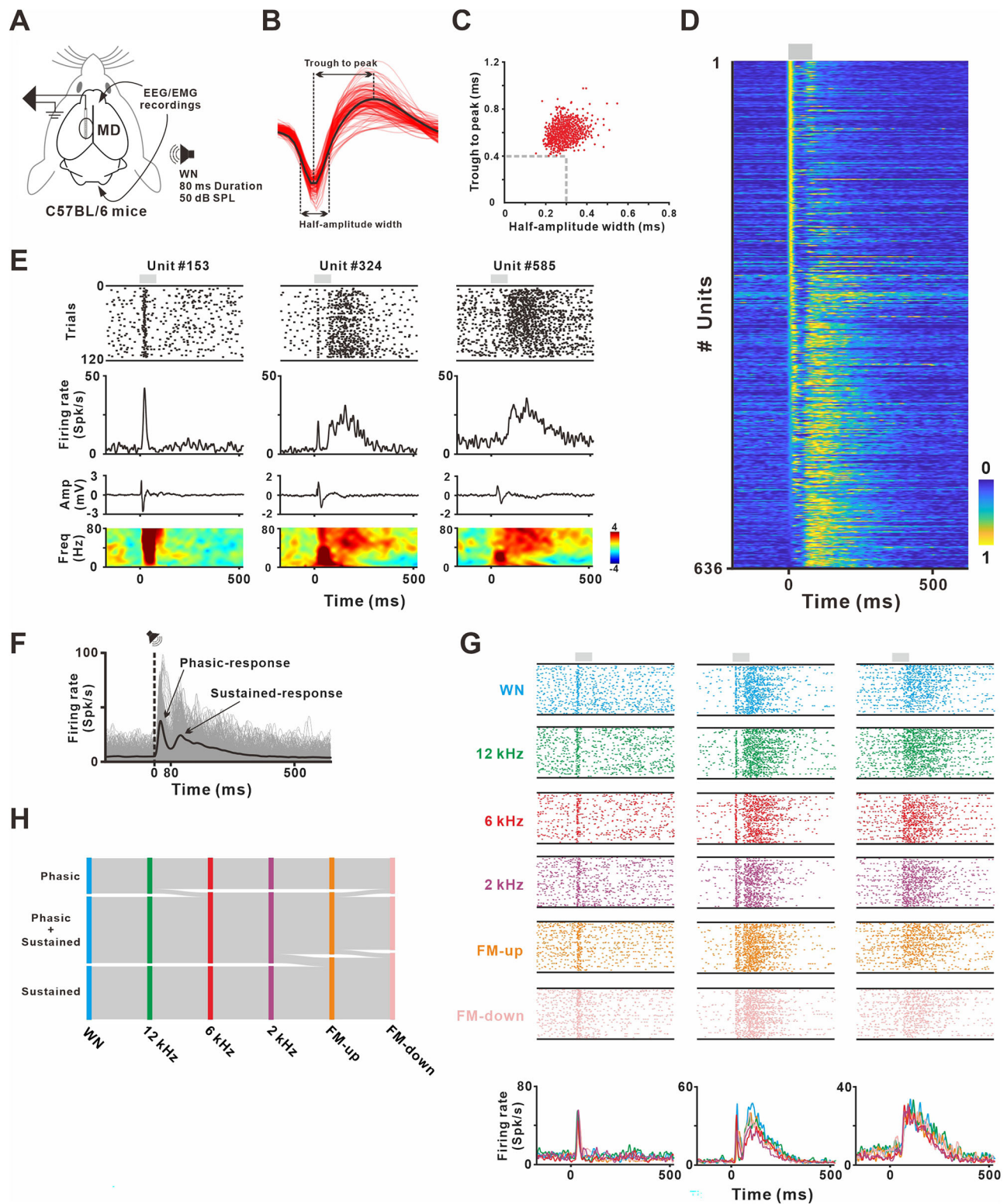
Fig. 2 | Characteristics of sound-evoked responses in MD neurons. A Schematic of the experimental setup showing a single-shank, 16-channel linear probe implanted into the unilateral MD, while presenting white noise (WN) stimuli to the contralateral side. Frontal EEG and neck EMG signals were simultaneously recorded using microwire electrodes. SPL, sound pressure level. Created by the authors. **B** Representative action potential (AP) waveforms of 636 units (from 12 mice) recorded in the MD. **C** Scatter plot of MD units over the half-amplitude width and the time from trough to peak. **D** Heatmap of the normalized peristimulus time histogram (PSTH) of SUAs. The gray rectangle indicates the presentation of sound stimulus. **E** Representative examples of SUAs recorded in the MD. From top to bottom: peri-event raster plots and PSTHs of the SUAs, as well as the traces and time-frequency spectrograms of simultaneously recorded LFP. **F** Individual (gray lines) and averaged (black line) PSTHs of the SUAS. The vertical dotted line marks the onset of the sound stimulus. **G** SUAs and PSTHs of three representative MD units in response to different auditory stimuli. **H** A Sankey diagram representing the changes in response patterns of MD units across various sound stimuli. N = 35 units from 6 mice.

electroencephalography (EEG) and neck electromyography (EMG) signals were recorded via microwire electrodes to monitor the level of arousal (Fig. S1). Figure 2B shows the action potential (AP) waveforms recorded from the MD. Based on measurements of half-amplitude width and trough-to-peak time[21], these APs were identified as regular-spiking (RS) units (Fig. 2C). The peristimulus time histograms (PSTHs) of single units activity (SUA) exhibited diverse patterns of sound-evoked response (Fig. 2D). Three representative examples are provided in the top panel of Fig. 2E. Unit #153 displayed a transient response to the sound stimulus with short latency, rapidly adapting to baseline, whereas Unit #585 exhibited a persistent response with longer latency. Unit #324 demonstrated both rapid transient and sustained responses. The waveforms and time-frequency spectrograms of the local field potential (LFP) are shown in the bottom panel of Fig. 2E. The LFP of Unit #153 showed a strong and rapid response at the presentation of sound stimulus, while the LFPs of Units #324 and #585 showed a long-lasting increase in gamma band power that persisted up to 500 ms after stimulus onset. The individual and averaged PSTHs (Fig. 2F) revealed two distinct peaks: one between 0 and 80 ms following stimulus onset, defined as the Phasic-response, and another between 80 and 500 ms, defined as the Sustained-response. These response patterns remained largely consistent despite variations in basic acoustic parameters, as demonstrated by three representative units in Fig. 2G and the population data in Fig. 2H.

Characteristics of sound-evoked response in the PFC, MRN and TRN neurons

We also recorded the auditory response of PFC neurons in awake mice by a single-shank, 16-channel linear probe (Fig. 3A). Based on AP morphology, 480 recorded units were classified, including 342 RS units and 138 fast-spiking (FS) units (Fig. 3B). Figure 3C shows the heatmaps of PSTHs for RS and FS units in response to white noise stimuli. Both RS and FS populations exhibited two distinct patterns: some units showed a Phasic-response followed by a Sustained-response, while others predominantly displayed a Sustained-response. The sound-evoked neuronal activity in the MRN is shown in Fig. 3D–F, with 381 RS units and 141 FS units recorded. Both RS and FS units exhibited a strong Phasic-response with minimal or no Sustained-response. The results from the TRN are shown in Fig. 3G–I. Given that previous studies have reported that the TRN is predominantly composed of FS GABAergic neurons[22,23], we included only 448 FS units for analysis (Fig. 3H). The PSTH heatmaps show that the majority of TRN units exhibit a strong Phasic-response followed by a relatively weaker Sustained-response (Fig. 3I). The individual and averaged PSTHs from the PFC, MRN, and TRN are presented in Fig. 3J. The averaged PSTH from these three brain regions also shows clear Phasic- and Sustained-responses occurring between 0–80 ms and 80–500 ms after stimulus onset (Fig. 3K).

Contribution of MRN on the sound-evoked response in the MD

We then applied electrophysiological recordings combined with optogenetic manipulation to investigate the role of MRN neural activity in the sound-evoked response of the MD. To determine whether MRN neurons projecting to the MD are inhibited by local GABAergic neurons, we injected AAV-retro-hSyn-cre-mCherry into the MD of VGAT-ChR2-EYFP mice. Three weeks later, Cre-inducible AAV-DIO-ChrimsonR was injected into the ipsilateral MRN, followed by implantation of an optical fiber above the MRN (Fig. 4A). Histological analysis revealed that mCherry+ MRN neurons projecting to the MD were surrounded by local EYFP+ GABAergic fibers (Fig. 4B). Electrophysiological recordings showed that the firing rate of local FS unit was not affected by 589-nm laser stimulation of the MRN, whereas it was elevated by 473-nm laser stimulation (Fig. 4C). In contrast, the firing rate of simultaneously recorded RS unit was increased by 589-nm laser stimulation and decreased by 473-nm laser stimulation (Fig. 4D). These results suggest that activation of GABAergic neurons in the MRN can significantly inhibit the activity of excitatory neurons projecting to the MD. Next, we inhibited the activity of MRN by optogenetically stimulating GABAergic neurons in the MRN of VGAT-ChR2-EYFP mice (MRN-silencing,

Fig. 4E). This approach has been shown in a previous study to produce nearly uniform inhibition of adjacent excitatory neurons[17]. Figure 4F presents the representative raster plots and PSTHs of MD units with (laser on) and without (laser off) MRN-silencing. MRN-silencing significantly suppressed the spontaneous firing rate of MD units (Fig. 4G). To investigate the regulatory effect of MRN-silencing on sound-evoked responses of MD units, we quantified the intensity of the Phasic- and Sustained-responses by calculating the area under the curve (AUC) for the PSTH peaks in the 0–80 ms and 80–500 ms windows following stimulus onset, respectively. We observed that both the AUC of the Phasic- (Fig. 4H) and Sustained-responses (Fig. 4I) were significantly reduced by MRN-silencing. Simultaneously recorded LFPs and the corresponding time-frequency spectrogram heatmaps are presented in Fig. 4J, K. We calculated the normalized power spectral density (PSD) of the LFP in the 0–80 ms (Fig. 4L) and 80–500 ms (Fig. 4M) windows following sound stimulation, and found that MRN-silencing significantly reduced oscillatory power across the delta, theta, alpha, beta, and gamma frequency bands in both time windows (Fig. 4N, O). These results indicate that the inputs from the MRN may serve as a source of the sound-evoked response in the MD.

Contribution of PFC on the sound-evoked response in the MD

Similarly, we expressed ChrimsonR in PFC neurons projecting to the MD in VGAT-ChR2-EYFP mice (Fig. 5A, B). 473-nm laser stimulation was used to activate local FS units in the PFC (Fig. 5C), which resulted in a significant decrease in the firing rate of RS units projecting to the MD (Fig. 5D). Then, we optogenetically stimulated GABAergic neurons in the PFC of VGAT-ChR2-EYFP mice (PFC-silencing) to investigate the role of PFC activity in the sound-evoked response of MD (Fig. 5E). Representative raster plots and PSTHs of MD units are shown in Fig. 5F. Statistical analysis revealed that PFC-silencing significantly reduced the spontaneous firing rate (Fig. 5G) and the Sustained-response of MD units (Fig. 5I), while the Phasic-response remained unaffected (Fig. 5H). Simultaneously recorded LFPs and corresponding time-frequency spectrogram heatmaps are presented in Fig. 5J, K. Statistical analysis showed that PFC-silencing had less effect on oscillatory power during the 0–80 ms window (Fig. 5L, N), but significantly reduced power across all frequency bands during the 80–500 ms window (Fig. 5M, O). These results suggest that PFC neural activity primarily contributes to the slow phase of the response in the MD, rather than the fast phase.

Modulation of TRN on the sound-evoked response in the MD

The TRN is a shell-like structure in the thalamus composed predominantly of GABAergic neurons, which project inhibitory inputs to the MD[19,20]. To investigate how TRN GABAergic inputs modulate sound-evoked responses in the MD, we optogenetically silenced TRN neurons by injecting AAV-DIO-eNpHR3.0-mCherry into the TRN of GAD2-Cre mice (TRN-silencing, Fig. 6A). Representative raster plots and PSTHs of MD units are shown in Fig. 6B. TRN-silencing significantly increased the spontaneous firing rate (Fig. 6C) and sound-evoked Sustained-response of MD units (Fig. 6E), while the Phasic-response remained unchanged (Fig. 6D). Simultaneous LFP analysis revealed that TRN-silencing had no significant effect on oscillatory power during the 0–80 ms post-stimulus window, but resulted in enhanced power across the delta to gamma frequency bands during the 80–500 ms window (Fig. 6F–K). Therefore, these results suggest that TRN GABAergic neurons negatively regulate the slow phase of sound-evoked response in the MD.

Discussion

The present study aimed to investigate the response patterns of the MD to auditory stimuli, as well as the contributions of upstream brain region inputs to the generation of sound-evoked responses in the MD. We identified two distinct response patterns in MD units: a Phasic-response characterized by transient burst firing with short
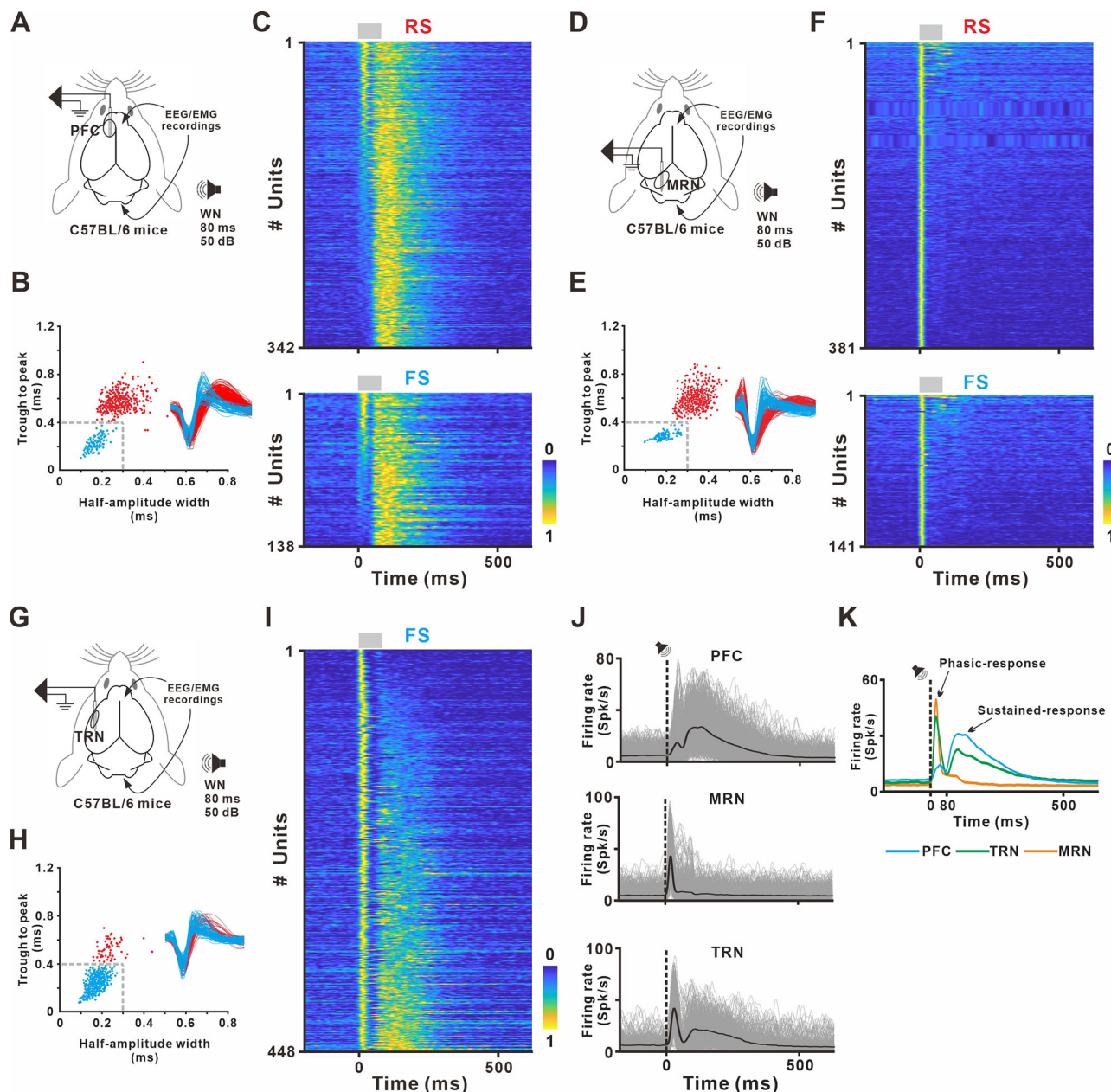
Fig. 3 | Patterns of sound-evoked response in the PFC, MRN and TRN.
A Schematic of the experimental setup. A single-shank, 16-channel linear probe was implanted into the PFC of awake mice, with WN stimuli presented to the contralateral side and simultaneous EEG and EMG recordings. Created by the authors. **B** Scatter plot of 480 PFC units (from 11 mice), based on half-amplitude width and the time from trough to peak. Inset: AP waveforms of RS units (n = 342, red) and FS units (n = 138, blue). **C** Heatmaps of PSTHs for RS and FS units in response to sound stimuli. **D–F** Sound-evoked neuronal activity in the MRN. N = 381 and 141 for RS and FS units, respectively, from a total of 12 mice. **G–I** Sound-evoked neuronal activity in the TRN. N = 448 for FS units from 10 mice. **J** Individual (gray lines) and averaged (black line) PSTHs from the PFC, MRN, and TRN. **K** Averaged PSTHs across brain regions show distinct Phasic- and Sustained-responses occurring between 0–80 ms and 80–500 ms following stimulus onset, respectively.

latency, and a Sustained-response marked by prolonged firing and enhanced LFP oscillatory power. These response patterns remained largely consistent despite variations in basic acoustic parameters. The Phasic-response was predominantly observed in the MRN, whereas the PFC exhibited a greater prevalence of the Sustained-response. Optogenetic inactivation of the MRN suppressed both Phasic- and Sustained-responses in the MD, while PFC inactivation selectively reduced the Sustained-response. In contrast, inactivation of the TRN enhanced the Sustained-response. Based on these findings, it can be inferred that the auditory responses in the MD primarily originate from three sources: the Phasic-response is primarily driven by bottom-up input from the MRN; the Sustained-response is jointly

controlled by bottom-up input from the MRN and top-down input from the PFC; and inhibitory input from the TRN negatively regulates the Sustained-response.

The MD serves as a crucial hub, extensively interconnected with multiple cortical and subcortical regions, playing a central role in the transmission and integration of sensory information within the thalamo-cortical pathway[24–26]. Previous electrophysiological studies in rodents and primates have demonstrated that a subset of MD neurons responds to auditory stimuli[16,17,27]. However, the detailed characteristics of sound-evoked responses in MD neurons have yet to be fully investigated. In the present study, we observed that auditory stimulation elicits two distinct response components in MD neurons: a short-latency, rapidly adapting
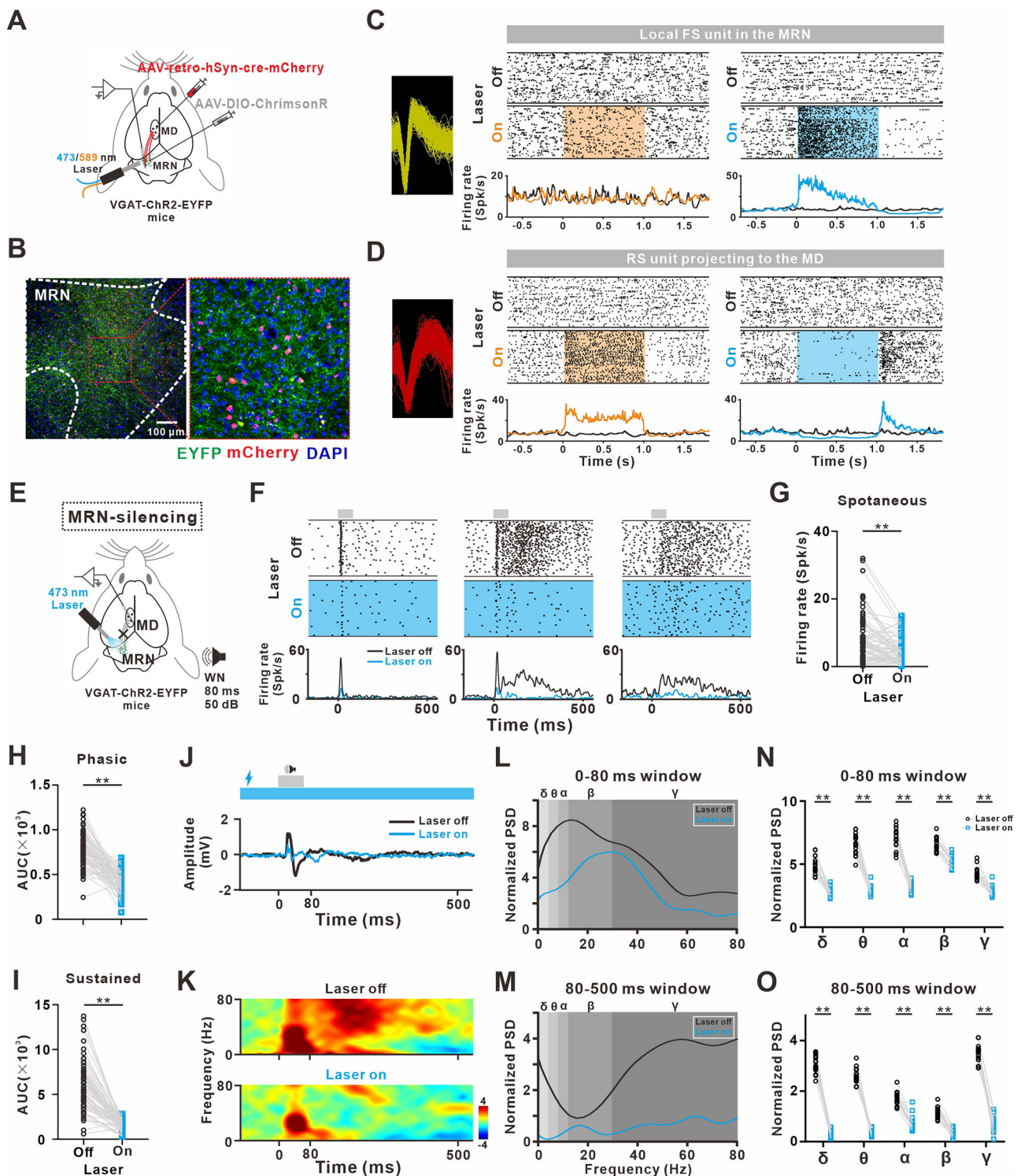
Fig. 4 | Role of the MRN in generating sound-evoked responses in the MD.
A Schematic of the experimental design showing local optogenetic activation of GABAergic neurons and simultaneous SUA recordings in the MRN of VGAT-ChR2-EYFP mice received AAV-retro-hSyn-cre-mCherry injection into the MD and AAV-DIO-ChrimsonR into the MRN. Created by the authors. B Histological image of EYFP/mCherry/DAPI labeling in the MRN. Green fluorescence indicates axonal fibers from EYFP-expressing local GABAergic neurons; red fluorescence marks MRN neurons projecting to the MD; and blue fluorescence represents nuclear staining (DAPI). Representative AP waveforms, raster plots, and PSTHs of a local FS unit (C) and a RS unit projecting to the MD (D) in the MRN under 589-nm and 473-nm laser stimulation. E Schematic for optogenetic inactivation of MRN (MRN-silencing), and simultaneous SUA and LFP recordings in the MD of VGAT-ChR2-EYFP mice. Created by the authors. F Raster plots and PSTHs of three representative MD neurons with and without MRN-silencing. Quantification of spontaneous firing rates (G) and AUC of sound-evoked Phasic- (H) and Sustained-responses (I) in MD neurons under different conditions. N = 72 units from 8 mice. Representative traces of LFP (J) and corresponding time-frequency spectrograms (K) in response to sound stimuli with or without MRN-silencing. Gray and blue rectangles indicate the presentation of sound and laser stimuli, respectively. Normalized PSD of LFPs in the 0–80 ms (L) and 80–500 ms (M) post-stimulus window. Gray shading indicates the frequency bands of delta, theta, alpha, beta, and gamma. Statistical analysis of normalized PSD across frequency bands in the 0–80 ms (N) and 80–500 ms window (O). N = 16 recording sessions from 8 mice. $^{**}P < 0.01$, as determined by a linear mixed-effects model (LME).
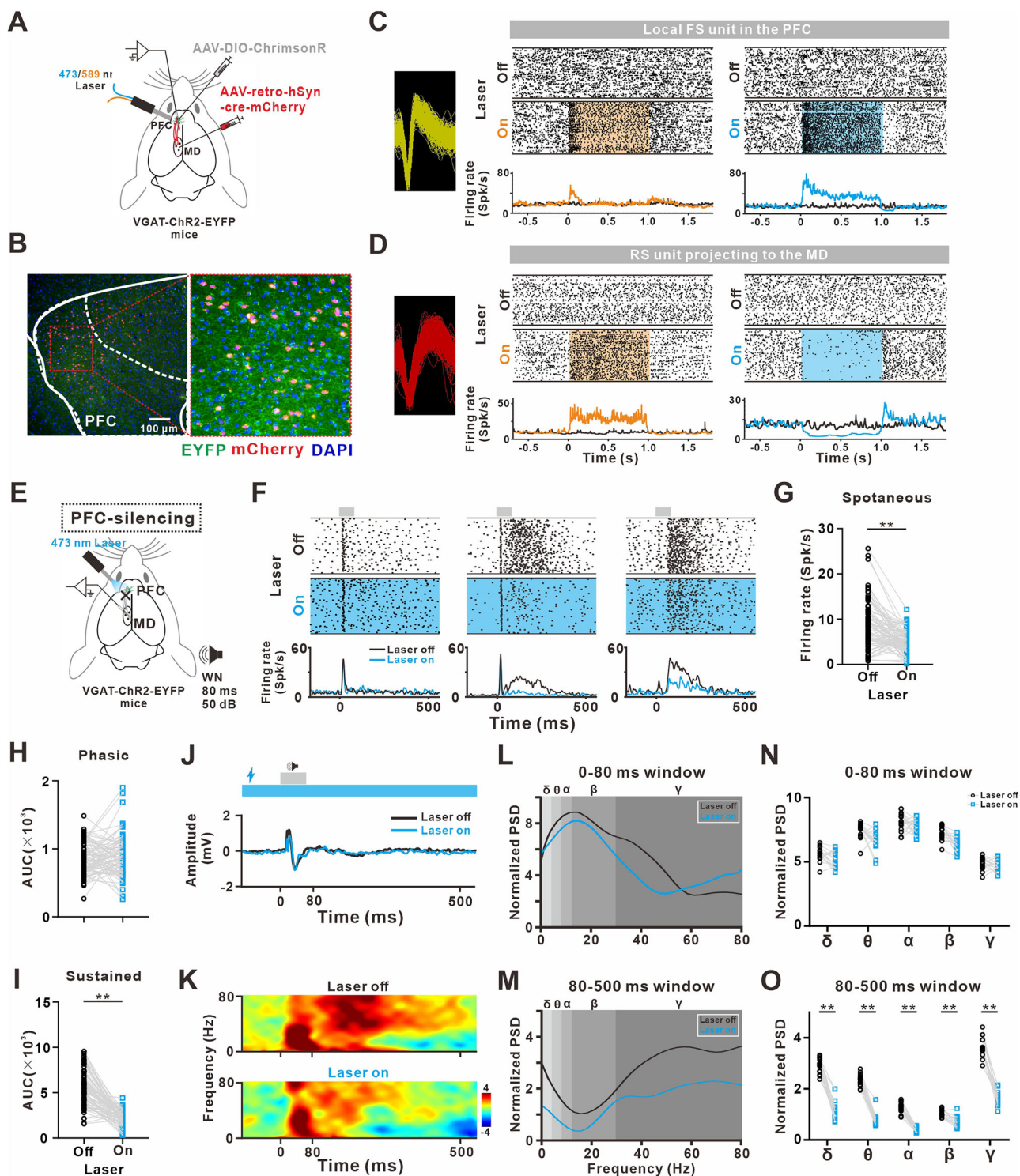
Fig. 5 | Role of PFC in modulating sound-evoked responses in the MD.
A Schematic of the experimental design showing local optogenetic activation of GABAergic neurons and simultaneous SUA recordings in the PFC of VGAT-ChR2-EYFP mice that received AAV-retro-hSyn-cre-mCherry injection into the MD and AAV-DIO-ChrimsonR into the PFC. Created by the authors. **B** Histological image showing EYFP/mCherry/DAPI labeling in the PFC. Representative AP waveforms, raster plots, and PSTHs of a local FS unit (**C**) and a RS unit projecting to the MD (**D**) in the PFC under 589-nm and 473-nm laser stimulation. **E** Schematic of optogenetic inactivation of PFC (PFC-silencing) and simultaneous SUA and LFP recordings in the MD of VGAT-ChR2-EYFP mice. Created by the authors. **F** Raster plots and

PSTHs of three representative MD neurons with and without PFC-silencing. Quantification of spontaneous firing rates (**G**) and AUC of sound-evoked Phasic- (**H**) and Sustained-responses (**I**) in MD neurons under different conditions. N = 83 units from 8 mice. Representative traces of LFP (**J**) and corresponding time-frequency spectrograms (**K**) in response to sound stimuli with and without PFC-silencing. Normalized PSD of LFPs in the 0–80 ms (**L**) and 80–500 ms (**M**) post-stimulus window. Statistical analysis of normalized PSD across frequency bands in the 0–80 ms (**N**) and 80–500 ms window (**O**). N = 16 recording sessions from 8 mice. $^{**}P < 0.01$, as determined by an LME.
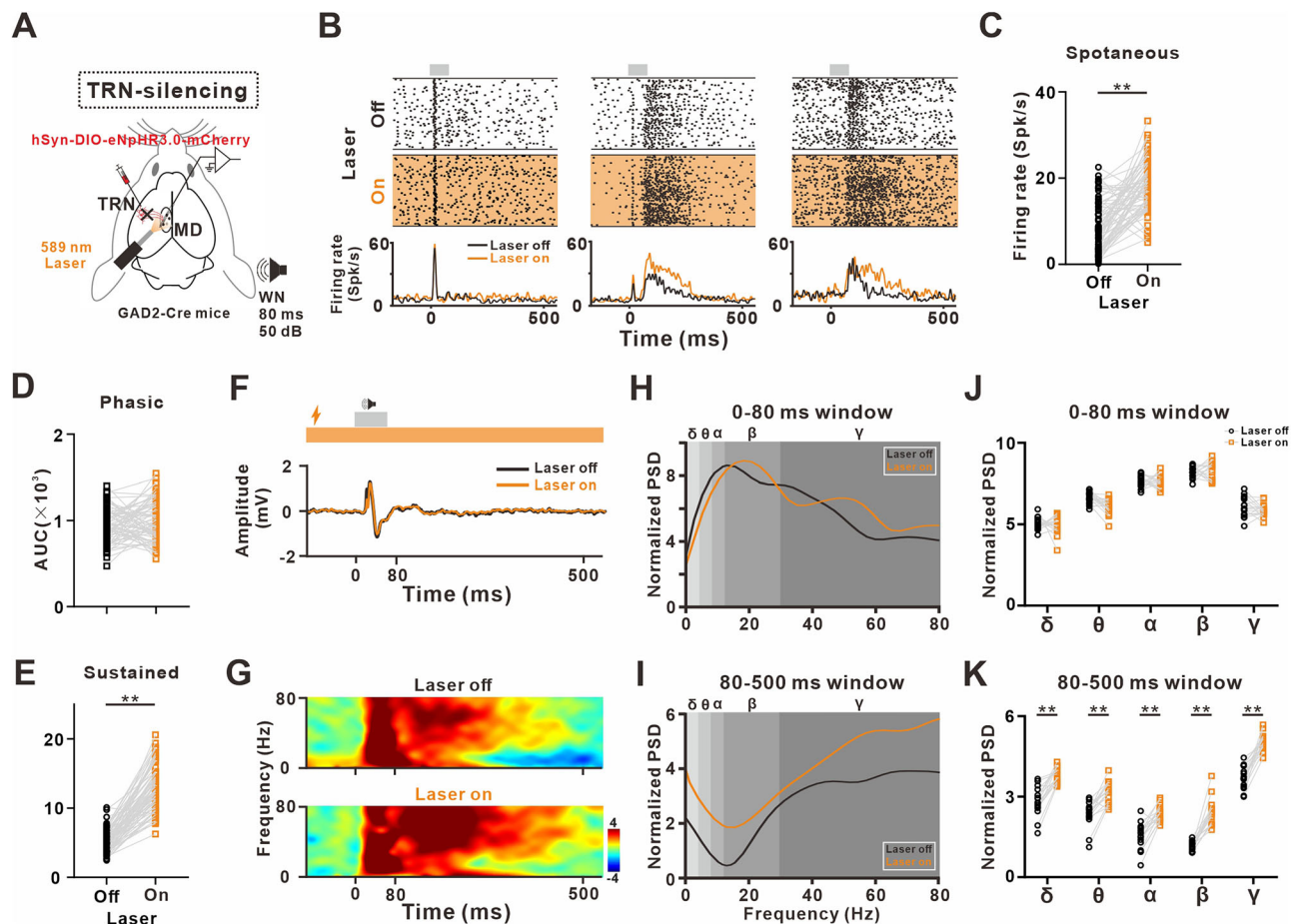
Fig. 6 | Role of TRN in modulating sound-evoked responses in the MD.
A Schematic for optogenetic inactivation of TRN (TRN-silencing), and simultaneous SUA and LFP recordings in MD of GAD2-Cre mice that received AAV-DIO-eNpHR3.0-mCherry injection in the TRN. Created by the authors. **B** Raster plots and PSTHs of three representative MD neurons with and without TRN-silencing. Quantification of spontaneous firing rates (**C**) and AUC of sound-evoked Phasic-(**D**) and Sustained-responses (**E**) in MD neurons under different conditions. N = 69 units from 8 mice. Representative traces of LFP (**F**) and corresponding time-frequency spectrograms (**G**) in response to sound stimuli with and without TRN-silencing. Normalized PSD of LFPs in the 0–80 ms (**H**) and 80–500 ms (**I**) post-stimulus window. Statistical analysis of normalized PSD across frequency bands in the 0–80 ms (**J**) and 80–500 ms window (**K**). N = 16 recording sessions from 8 mice. $^{**}P < 0.01$, as determined by an LME.

spiking response accompanied by transient LFP fluctuations, and a long-latency, slowly adapting spiking response associated with delayed gamma-band oscillations. Analogous patterns of Phasic- and Sustained-responses have been reported in MD neurons in response to nociceptive and visual stimuli[27–30]. Phasic-response neurons are characterized by the presence of fast-activating sodium channels, enabling rapid depolarization and the swift generation of action potentials. Their responses typically diminish shortly after stimulus onset due to rapid repolarization mediated by potassium channels. These neurons often receive direct inputs from the brainstem and first-order sensory thalamus, resulting in short latencies and brief response durations. In contrast, Sustained-responses arise from continuous synaptic input and recurrent excitatory activity within neural circuits. Sustained-response neurons generally integrate input from multiple central regions, with signals relayed through cortical and subcortical areas, leading to long latencies and extended response durations. Transient neuronal responses to sensory stimuli are thought to facilitate the rapid detection of external signals and initiate appropriate behavioral reactions[31,32]. Rapid adaptation helps maintain sensitivity to novel stimuli while preventing sensory overload caused by redundant information[33,34]. Furthermore, sensory-evoked gamma oscillations are believed to enhance information transmission and inter-regional coordination, supporting efficient neural communication, arousal, and attentional performance[35–37]. Together, our findings emphasize the multidimensional role of the MD in sensory integration and attentional regulation.

Anatomical studies have shown that the MD receives input from the MRN, a key component of the brainstem's ascending projection system[5,38,39]. Auditory inputs to the MRN primarily originate from the central and dorsal nuclei of the inferior colliculus[40]. Additionally, the auditory responsiveness of the MRN is modulated by dopaminergic inputs from the pontine reticular formation and the ventral tegmental area[41]. Previous research has demonstrated that auditory stimuli can elicit a transient increase in SUA in the MRN[5]. Consistently, our current findings revealed that the vast majority of MRN neurons displayed a Phasic-response pattern, similar to the early components of sound-evoked activity observed in MD neurons.

The presence of direct neural projections from the PFC to the MD has been well-established[4,42]. Previous electrophysiological studies in both awake and anesthetized mice have demonstrated that PFC neurons exhibit a continuous increase in SUA in response to broadband noise stimuli, lasting for approximately 500 ms following stimulus offset[43,44]. In current study, we also observed that the majority of PFC neurons displayed a prolonged, sound-evoked enhancement in SUA, corresponding to the Sustained-response in MD neurons.

Optogenetic inactivation of MRN neuronal activity suppressed both the Phasic- and Sustained-response in MD neurons. Optogenetic inactivation of PFC neuronal activity significantly suppressed the Sustained-response, while having minimal impact on the Phasic-response. Based on these observations, we hypothesize that the attenuation of the MD Phasic-response following MRN-silencing is due to the blockade of phasic input

from the MRN. On the other hand, the Phasic-response in the MD triggers sustained neural reverberation within the MD-PFC loop, which leads to the formation of the Sustained-response in the MD. Therefore, both MRN-silencing and PFC-silencing can result in the attenuation of the Sustained-response in the MD. These results imply that the auditory responses of the MD may originate from the MRN. Prior behavioral experiments have suggested that ascending auditory projections from the MRN to the MD are involved in the transition from sleep to wakefulness[39] as well as in triggering behavioral responses to auditory stimuli[5]. Therefore, the MRN-MD pathway may contribute to the detection and transmission of auditory signals. Additionally, persistent top-down input from the PFC also serves as a key contributor to the Sustained-response in MD neurons. Previous studies in rodents have shown that sustained SUA and gamma-band oscillation in the PFC, evoked by visual and nociceptive cues, are closely associated with perceptual attention, facilitating the suppression of irrelevant information and the selective focus attention on stimuli of interest[45,46]. By analogy, the Sustained-responses in the MD driven by PFC-MD pathway may also contribute to auditory attention functions.

The TRN, located at the periphery of the thalamus, is characterized by a substantial population of GABAergic neurons[47,48]. As a key modulator within the thalamo-cortical network, the TRN regulates the transmission of sensory information, including auditory and visual cues, and exerts a sensory gating function[49–51]. A previous study reported that TRN neurons respond to auditory stimulation with two distinct peaks in neuronal discharge: a fast peak, characterized by significant neuronal activity but short duration, and a slow peak, characterized by relatively weaker neuronal activity but longer duration[52]. In line with these findings, our study also identified a mixture of Phasic- and Sustained-responses in TRN neurons. Optogenetic inactivation of TRN neuronal activity selectively enhanced the Sustained-response in MD neurons, accompanied by an increase in oscillatory power across delta to gamma band frequencies. In contrast, the Phasic-response in the MD—largely driven by bottom-up input from the MRN—remained unaffected. These findings suggest that the TRN primarily exerts a suppressive effect on the Sustained-response in the MD, potentially contributing to auditory gating by limiting continuous attention to irrelevant auditory stimuli.

In conclusion, the MRN-MD bottom-up pathway, which transmits the Phasic-response, may contribute to the detection and transmission of auditory signals. The PFC-MD top-down pathway, contributing to the Sustained-responses, may be involved in auditory attention functions. Inhibitory regulation from the TRN may exert gating effects on the PFC-MD top-down input, helping to modulate attention to irrelevant stimuli. Our findings elucidate the potential neural circuitry mechanisms underlying auditory responses in the MD and offer new insights into its role in integrating sound information and regulating auditory cognition.

Several limitations should be acknowledged in the present study. First, we did not utilize naturalistic sounds to elucidate the MD's involvement in higher-order auditory processing. Second, we did not selectively optogenetically manipulate the projections from the PFC, MRN, and TRN to the MD, and therefore, cannot determine whether the observed effects are due to direct connections or indirect network effects. These limitations need to be addressed in future research.

Materials and methods
Animals
C57BL/6 mice were obtained from Vital River Laboratory (Beijing, China). VGAT-ChR2-EYFP and GAD2-Cre mice were obtained from The Jackson Laboratory (stock numbers: 014548 and 010802, respectively). Experiments were conducted on adult mice of both sexes, aged 6–8 weeks and weighing 18–25 g. Animals were housed at a constant temperature of $22 \pm 1\,°C$ and humidity (30–50%) under a 12-h light / 12-h dark cycle, with food and water available ad libitum. All experiments were conducted in a blinded manner, with the investigators responsible for data collection and analysis remaining blinded to the experimental conditions. All procedures were performed in compliance with the National Institutes of Health guide for the Care and Use of Laboratory Animals (NIH Publications No. 8023, revised 1978). All

experimental protocols were approved by the Animal Ethics Committee of China Medical University (No. CMU2019126).

Surgical procedures and electrode implantation
Mice were initially anesthetized in an induction chamber with 3% isoflurane and then fixed in a stereotaxic apparatus (#68001, RWD Life Science, Shenzhen, China), with continuous administration of 1.5% isoflurane to maintain anesthesia. Body temperature was maintained at 37 °C throughout the surgery using a heating pad. A local analgesic composed of a 1:1 mixture of lidocaine (4%) and bupivacaine (0.25%) was administered subcutaneously below the scalp prior to the surgical procedure. After shaving the hair and disinfecting the incision site with medical alcohol, the scalp was incised, and the underlying connective tissue was gently removed. The skull surface was cleaned with a 5% hydrogen peroxide solution and dried using an air puffer. The skull was positioned such that bregma and lambda landmarks were aligned along the anteroposterior (AP), mediolateral (ML) and dorsoventral (DV) axes. For EEG and EMG recordings to assess brain arousal states, a stainless-steel screw was implanted into the surface of the PFC (AP = +1.94 mm, ML = –0.50 mm, DV = –2.70 mm) based on the standardized mouse brain atlas (The Mouse Brain in Stereotaxic Coordinates, 3rd edition). The screw was connected using Teflon-coated silver microwires (#785500, A-M Systems, WA, USA). Two stainless-steel wires (#793200, A-M Systems, WA, USA) were inserted into the neck musculature. For acute recording with a multichannel silicon probe, the locations of the MD (AP = –1.55 mm, ML = +0.50 mm, DV = –3.00 mm), TRN (AP = –0.82 mm, ML = +1.50 mm, DV = –3.20 mm), PFC and MRN (AP = –4.04 mm, ML = +1.20 mm, DV = –3.10 mm) in the left hemisphere were marked on the skull surface with ink. A ~ 1 mm craniotomy was performed over the cerebellum, and two stainless-screws were inserted and connected using Teflon-coated silver microwires, serving as the ground and reference. The opposite ends of the microwires were soldered to a pin connector, which was secured to the cranium of the right hemisphere with dental cement. A custom-designed head post was affixed to the occipital and nasal bones. Following surgery, mice were returned to single-housed cages, and antibiotics (enrofloxacin, 10 mg/kg) and analgesic (carprofen, 5 mg/kg) were added to their drinking water. Animals were allowed to recover for at least 2 weeks before undergoing any further procedures.

Viral injections and optic fiber implantation
Viral injections were performed using a stereotactic frame under isoflurane anesthesia, as previously described. A small craniotomy (~1 mm in diameter) was drilled under a microscope, and AAV vectors were delivered through a beveled glass micropipette (tip diameter: 30–40 μm) attached to a micro-syringe pump (Pump 11 Elite, Harvard Apparatus, Holliston, USA) at a rate of 20 nl/min. After the injection, the pipette was left in place for an additional 10 min before being slowly retracted. For retrograde monosynaptic labeling of neurons projecting to the MD, AAV-retro-hSyn-mCherry (300 nl, BrainVTA, Wuhan, China) was injected unilaterally into the MD (coordinates as described above). For optogenetic labeling of MRN/PFC neurons projecting to the MD, AAV-retro-cre-hSyn-mCherry (300 nl, BrainVTA, Wuhan, China) was injected unilaterally into the MD. Three weeks later, AAV-DIO-ChrimsonR (300 nl, BrainVTA, Wuhan, China) was injected into the ipsilateral MRN or PFC. For optogenetic inactivation of excitatory neurons in the MRN or PFC, an optical fiber (200 μm core diameter and 0.39 numerical aperture, Newdoon Technology, Hangzhou, China) was implanted into the MRN or PFC of VGAT-ChR2-EYFP mice. For inactivation of GABAergic TRN inputs to the MD, GAD2-Cre mice were injected unilaterally with AAV-DIO-eNpHR3.0-mCherry into the TRN, with an optic fiber inserted at a ~ 30° angle targeting the ipsilateral MD. The optical fibers were secured to the skull using dental cement and skull screws. An unexpected adverse event occurred when two animals exhibited signs of infection at the surgical site following implantation of the optogenetic fiber. These animals were excluded from further analysis, and appropriate

veterinary care was provided. The infection was promptly treated, and no further complications were observed in the remaining animals.

Acoustic and optogenetic stimulation

Waves of broadband white noise (4–44 kHz), pure-tone (2, 6 and 12 kHz), upward and downward frequency-modulated sound (FM, 128 Hz-16 kHz) were generated using custom MATLAB scripts. Each sound stimulus had a duration of 80 ms. The signal was transferred via an A/D converter board (PCI-6052E, National Instruments, Austin, Texas, USA), and played through a free-field speaker (K701, AKG, Vienna, Austria) positioned adjacent to the ear contralateral to the recording site. Sound intensity was set to 50 dB sound pressure level (SPL) and measured at the position of the animal's ear using a sound level meter (Bruel & Kjaer type 2238, Naerum, Denmark). During sessions to record sound-evoked responses in the target brain regions, a total of 120 trials of stimuli were delivered with randomly varied interstimulus intervals ranging from 6 to 9 s.

Optogenetic stimulation was used to precisely control the activity of ChR2/eNpHR3.0-expressing neurons and investigate their role in neural circuit regulation. In this study, optogenetic stimuli were generated via a pulse stimulator (Newdoon Inc., Hangzhou, China) and delivered to the brain through an optic fiber cable (1 m length, 200-μm core diameter, Newdoon Inc., Hangzhou, China). The laser intensity was measured by an optical power meter (Newdoon Inc., Hangzhou, China) and calibrated to 0.83–3.33 mW/mm^2 at the fiber tip. During the pre-experimental phase, we systematically determined the optimal optogenetic stimulation intensity by testing a range of light intensities (5-20 mW) in a stepwise manner. The optimal intensity was defined as the level at which more than 50% of recorded units exhibited changes in firing rate exceeding the mean ±2 standard deviations (SD) of their baseline spontaneous activity within a single recording session. To ensure the specificity of regional manipulation and avoid thermal interference, the maximum laser intensity was limited to 20 mW. We observed that 473-nm laser activation of GABAergic neurons effectively suppressed the activity of local RS units; however, upon cessation of the laser, RS units exhibited a pronounced rebound firing (Figs. 4D, 5D). To prevent this rebound activity from confounding sound-evoked responses, which could obscure the interpretation of MD neuronal firing patterns, we applied a continuous 1000 ms laser pulse beginning 250 ms prior to the onset of the broadband noise, thereby fully encompassing the sound stimulus duration. In VGAT-ChR2-EYFP mice injected with optogenetic virus, 589-nm laser stimulation was applied to the PFC or MRN to identify neurons projecting to the MD. 473-nm laser stimulation was used to activate local GABAergic neurons in the PFC or MRN. Additionally, 589-nm laser stimulation was applied to the MD of GAD2-Cre mice to selectively inactivate the inhibitory inputs from the TRN to the MD.

Electrophysiological recordings

All recordings were conducted in a custom-built acoustic isolation booth. Prior to the recording experiments, mice were acclimated to the environment by spending 3 h per day in the recording room for 4 consecutive days. During this period, the animals were affixed atop a free-spinning treadmill via a custom-designed head post secured to the skull. On the 5th day, the mice were placed in the recording booth and anesthetized with 3% isoflurane. A craniotomy of approximately 2 mm in diameter was performed above the targeted brain areas, previously marked with ink. A recording chamber was constructed around the craniotomy using UV-cured cement. The mice were allowed sufficient time to recover from anesthesia. Neuronal activity in the MD, PFC, MRN and TRN was recorded separately using a single-shank, 16-channel silicon probe (A1×16-3.8mm-50-177, Neuro-Nexus, MI, USA). Recording sites were linearly arranged along the shank, with an inter-site spacing of 50 μm. The distance from the probe tip to the first recording site was 25 μm. The probe was mounted on a remotely controlled micromanipulator (MO-1, Narishige, Tokyo, Japan) and gradually lowered into the target areas, guided by electrophysiological signals and anatomical landmarks based on the mouse brain atlas. Once the SUA stabilized, the recording session commenced. The recording order was

randomized daily, with each animal recorded at a different time each test day. Signals from the probe were routed to a multichannel preamplifier (RA16PA, Tucker-Davis Technologies, TDT; Alachua, FL, USA) and subsequently to a digital signal processing module (RZ-2; TDT). Raw electrophysiological data were bandpass-filtered at 0.5–300 Hz for LFPs and 300–5000 Hz for SUAs. The neural waveforms were digitized by the OpenEx software of TDT and SUAs were detected using principal component analysis (PCA)[17]. After each session, the chamber was cleaned, filled with ointment, and sealed with UV-cured cement. Before each subsequent recording session, the chamber was reopened and reconstructed under isoflurane anesthesia. Typically, 2–5 recording sessions were performed per animal over a 2 week period. Following the final recording session, animals were euthanized, and probe placement was verified via histological brain sectioning.

Analysis of the electrophysiological data

To identify the arousal state of mice during the recordings, we simultaneously recorded frontal EEG and neck EMG data. Using a heuristic automated approach combined with independent visual inspection, we categorized EEG data into wake, non-rapid eye movement (NREM), and rapid eye movement (REM) episodes (Supplementary Fig. 1). Spectrograms were first computed from the recorded EEG signals, and PCA was conducted to each spectrogram. The first principal component (PC1) primarily reflected low-frequency power, with the weights of frequencies <25 Hz being opposite in sign to those of frequencies in the gamma range. By analyzing the bimodal distribution of PC1 magnitudes, a threshold was determined at the trough between the two peaks, enabling the classification of each second as NREM (high PC1 power) or "other" (low PC1 power). Subsequently, the "other" epochs were further classified based on a narrow-band theta power ratio (5–10 Hz/2–16 Hz) and EMG measures. The original EMG signals were rectified and smoothed. Typical EMG segments were selected from both the high muscle tone awake state and the atonic sleep state, with five 1 s segments chosen from each condition. The average amplitude for each state was calculated, and the midpoint of these values was used as the threshold for classification. To avoid sudden movement artifacts, a high muscle tone state was only considered when the EMG amplitude remained above the threshold for more than 1 s. Conversely, a low muscle tone state was defined when the EMG amplitude remained below the threshold for more than 1 s. Epochs exhibiting high theta power and low muscle tone were designated as REM. The remaining epochs were categorized as wake episodes. A mouse was considered to be in the awake state if the proportion of wake epochs exceeded 80% during a given recording session. Based on this criterion, 88.23% of MD sessions (75/85), 85.48% of PFC sessions (53/62), 78.46% of TRN sessions (51/65), and 83.1% of MRN sessions (59/71) were included in the subsequent analyses.

An 800 ms peristimulus epoch (–200 to 600 ms relative acoustic stimulus onset) of SUAs was extracted across all trials within each recording session. Sessions in which more than 50% of trials were contaminated by gross artifacts or data were acquired from damaged electrodes were discarded. Units with a signal-to-noise ratio greater than 3:1 and a peak-to-trough amplitude variation of less than 20% were included. Units showing significant drift or instability were excluded to ensure the reliability and consistency of the neuronal data. PSTHs were constructed by calculating the instantaneous firing rate (1-ms bin) for each epoch from SUA, followed by smoothing with a 5-ms Gaussian sliding window. PSTHs were averaged across trials to obtain the mean PSTH per unit. The spontaneous firing rate was measured during the pre-stimulus baseline period (–200 to 0 ms). A Phasic-response was defined as a response in which the maximum firing rate within the 0–80 ms post-stimulus window exceeded the mean +2 SD of the pre-stimulus spontaneous firing rate. A Sustained-response was defined as a response in which the maximum firing rate within the 80–500 ms post-stimulus window exceeded the mean +2 SD of the pre-stimulus spontaneous firing rate and persisted for more than 100 ms. The intensity of Phasic- and Sustained-responses was quantified by calculating the AUC of the mean PSTH within the 0–80 ms and 80–500 ms windows, respectively.

LFP signals were downsampled to 1 kHz. Trial-based spectral analysis of LFPs were performed using a wavelet-based algorithm implemented in the EEGLAB toolbox (http://sccn.ucsd.edu/eeglab/index.php). Spectral-temporal power was averaged across all trials within each recording session. For each session, LFP power was computed to generate a spectral-temporal representation using the multitaper method provided by EEGLAB. Results were presented as a relative estimation of the ratio between the values following acoustic stimulus onset and the baseline value. Frequency bands were defined as follows: δ (0.5–4.0 Hz), θ (4.1–8.0 Hz), α (8.1–12.0 Hz), β (12.1–30.0 Hz) and γ (30.1–80.0 Hz). PSD was estimated using Welch's method. Specifically, LFP data were divided into several segments with 50% overlap. Each segment was windowed by a Hamming window, and the periodogram of each windowed segment was obtained using a Fast Fourier Transform. All periodogram were averaged to obtain the final Welch PSD values for each participant. Average power within the five predefined frequency bands was used for further analysis.

Histology

After completion of all experiments, each mouse was anesthetized with pentobarbital (100 mg/kg) and perfused transcardially with 20 ml phosphate-buffered saline (PBS), followed by 20 ml of 4% paraformaldehyde. Brains were extracted and placed in a fixative solution at 4 °C for 48 h. Brain sections were cut at 30 μm thickness via a freezing microtome (CM1950; Leica, Wetzlar, Germany). The slices were then washed 3 times in PBS, mounted onto glass slides, and coverslipped with 4′,6-diamidino-2-phenylindole (DAPI, Cat# 0100-20, Southern Biotech, Birmingham, AL, USA). For immunofluorescence analysis, brain slices were first treated with a blocking buffer containing 10% donkey serum in PBS for 1 h at room temperature to minimize nonspecific antibody binding. The slices were then incubated at 4 °C for 24 h with one of the following primary antibodies diluted in blocking solution: anti-vesicular glutamate transporter 2 (Vglut2, 1:200 dilution, ab216463, Abcam, USA) or anti-glutamic acid decarboxylase 67 (Gad67, 1:500 dilution, A2938, ABclonal, China). After 3 rinses in PBS, slices were incubated with species-appropriate, fluorophore-conjugated secondary antibodies (1:200 dilution; Proteintech, China) for 2 h at room temperature. Finally, slices were mounted with a DAPI-containing mounting medium for nuclear visualization. The recording probe track, virus injection site, and retrogradely labeled neurons were verified under a fluorescence microscope (BX53, Olympus, Tokyo, Japan) according to the Paxinos and Franklin mouse brain atlas.

Statistics and reproducibility

Statistical analysis was performed using GraphPad Prism 9.0 (graphpad.com) and MATLAB. The normality of the data was assessed using the Shapiro-Wilk test. Comparisons of the proportions of Vglut2$^+$ and Gad 67$^+$ cells in the MD were analyzed using Student's t test. Fisher's exact test was used to analyze the impact of different auditory stimulus types on the response patterns of MD neurons, with Holm-Bonferroni correction applied to control for the false positive rate associated with multiple comparisons. A linear mixed-effects model (LME) was employed to analyze the spontaneous firing rate, the AUC of Phasic- and Sustained-response, and the normalized PSD of LFPs across different optogenetic conditions, accounting for variability among individual mice. All values are reported as mean ± standard error of the mean (SEM), unless otherwise stated. Statistical significance was defined as $P < 0.05$.

To ensure reproducibility, each experiment was independently repeated at least three times under identical conditions. Biological replicates were defined as independent experimental trials performed using distinct biological samples. For in vivo experiments, each replicate was conducted using a separate group of animals to minimize individual variability. Sample sizes were determined based on prior literature and, where applicable, guided by power analyses to ensure sufficient statistical power. Experiments without formal statistical testing were still repeated across multiple biological replicates to confirm reproducibility. The exact number of sample sizes for each experiment are provided in the corresponding figure legends.

Reporting summary

Further information on research design is available in the Nature Portfolio Reporting Summary linked to this article.

Data availability

The data that support the findings of this study are available from Supplementary Data 1. Additional information is available from the corresponding author upon reasonable request.

Code availability

The custom codes used for analyzing data are available at http://github.com/Aaronwong1219/PSTH.

References

1. Halassa, M. M. & Kastner, S. Thalamic functions in distributed cognitive control. *Nat. Neurosci.* **20**, 1669–1679 (2017).
2. Kuroda, M., Yokofujita, J. & Murakami, K. An ultrastructural study of the neural circuit between the prefrontal cortex and the mediodorsal nucleus of the thalamus. *Prog. Neurobiol.* **54**, 417–458 (1998).
3. Ferrarelli, F. & Tononi, G. Reduced sleep spindle activity point to a TRN-MD thalamus-PFC circuit dysfunction in schizophrenia. *Schizophr. Res* **180**, 36–43 (2017).
4. Parnaudeau, S., Bolkan, S. S. & Kellendonk, C. The mediodorsal thalamus: An essential partner of the prefrontal cortex for cognition. *Biol. Psychiatry* **83**, 648–656 (2018).
5. Inagaki, H. K. et al. A midbrain-thalamus-cortex circuit reorganizes cortical dynamics to initiate movement. *Cell* **185**, 1065–1081.e1023 (2022).
6. DeNicola, A. L., Park, M. Y., Crowe, D. A., MacDonald, A. W. 3rd & Chafee, M. V. Differential roles of mediodorsal nucleus of the thalamus and prefrontal cortex in decision-making and state representation in a cognitive control task measuring deficits in schizophrenia. *J. Neurosci.* **40**, 1650–1667 (2020).
7. Huang, A. S., Mitchell, J. A., Haber, S. N., Alia-Klein, N. & R. Z. Goldstein. The thalamus in drug addiction: from rodents to humans. *Philos. Trans. R Soc. Lond. B Biol. Sci.* **373**, https://doi.org/10.1098/rstb.2017.0028 (2018).
8. Georgescu, I. A., Popa, D. & Zagrean, L. The anatomical and functional heterogeneity of the mediodorsal thalamus. *Brain. Sci.* **10**, https://doi.org/10.3390/brainsci10090624 (2020).
9. Mitchell, A. S. The mediodorsal thalamus as a higher order thalamic relay nucleus important for learning and decision-making. *Neurosci. Biobehav Rev.* **54**, 76–88 (2015).
10. Minzenberg, M. J., Laird, A. R., Thelen, S., Carter, C. S. & Glahn, D. C. Meta-analysis of 41 functional neuroimaging studies of executive function in schizophrenia. *Arch. Gen. Psychiatry* **66**, 811–822 (2009).
11. Pitel, A. L., Segobin, S. H., Ritz, L., Eustache, F. & Beaunieux, H. Thalamic abnormalities are a cardinal feature of alcohol-related brain dysfunction. *Neurosci. Biobehav Rev.* **54**, 38–45 (2015).
12. Pitel, A. L. et al. Macrostructural abnormalities in Korsakoff syndrome compared with uncomplicated alcoholism. *Neurology* **78**, 1330–1333 (2012).
13. Courtiol, E. & Wilson, D. A. The olfactory thalamus: unanswered questions about the role of the mediodorsal thalamic nucleus in olfaction. *Front Neural Circuits* **9**, 49 (2015).
14. Mukherjee, A., Lam, N. H., Wimmer, R. D. & Halassa, M. M. Thalamic circuits for independent control of prefrontal signal and noise. *Nature* **600**, 100–104 (2021).

15. Marton, T. F., Seifikar, H., Luongo, F. J., Lee, A. T. & Sohal, V. S. Roles of prefrontal cortex and mediodorsal thalamus in task engagement and behavioral flexibility. *J. Neurosci.* **38**, 2569–2578 (2018).

16. Oyoshi, T., Nishijo, H., Asakura, T., Takamura, Y. & Ono, T. Emotional and behavioral correlates of mediodorsal thalamic neurons during associative learning in rats. *J. Neurosci.* **16**, 5812–5829 (1996).

17. Wang, S. et al. Cortical and thalamic modulation of auditory gating in the posterior parietal cortex of awake mice. *Cereb. Cortex* **33**, 6742–6760 (2023).

18. Vertes, R. P., Linley, S. B. & Hoover, W. B. Limbic circuitry of the midline thalamus. *Neurosci. Biobehav Rev.* **54**, 89–107 (2015).

19. El Boukhari, H., Ouhaz, Z., Ba-M'hamed, S. & Bennis, M. Early lesion of the reticular thalamic nucleus disrupts the structure and function of the mediodorsal thalamus and prefrontal cortex. *Dev. Neurobiol.* **79**, 913–933 (2019).

20. Okada, M., Fukuyama, K., Nakano, T. & Ueda, Y. Pharmacological discrimination of effects of MK801 on thalamocortical, mesothalamic, and mesocortical transmissions. *Biomolecules* **9**, https://doi.org/10.3390/biom9110746 (2019).

21. Wang, S. et al. Repeated postnatal sevoflurane exposure impairs social recognition in mice by disrupting GABAergic neuronal activity and development in hippocampus. *Br. J. Anaesth.* **133**, 810–822 (2024).

22. Tassin, V. et al. Phasic and tonic mGlu7 receptor activity modulates the thalamocortical network. *Front Neural Circuits* **10**, 31 (2016).

23. Halassa, M. M. et al. State-dependent architecture of thalamic reticular subnetworks. *Cell* **158**, 808–821 (2014).

24. Goldman-Rakic, P. S. & Porrino, L. J. The primate mediodorsal (MD) nucleus and its projection to the frontal lobe. *J. Comp. Neurol.* **242**, 535–560 (1985).

25. Alcaraz, F., Marchand, A. R., Courtand, G., Coutureau, E. & Wolff, M. Parallel inputs from the mediodorsal thalamus to the prefrontal cortex in the rat. *Eur. J. Neurosci.* **44**, 1972–1986 (2016).

26. Bolkan, S. S. et al. Thalamic projections sustain prefrontal activity during working memory maintenance. *Nat. Neurosci.* **20**, 987–996 (2017).

27. Tanibuchi, I. & Goldman-Rakic, P. S. Dissociation of spatial-, object-, and sound-coding neurons in the mediodorsal nucleus of the primate thalamus. *J. Neurophysiol.* **89**, 1067–1077 (2003).

28. Dostrovsky, J. O. & Guilbaud, G. Nociceptive responses in medial thalamus of the normal and arthritic rat. *Pain* **40**, 93–104 (1990).

29. Whitt, J. L., Masri, R., Pulimood, N. S. & Keller, A. Pathological activity in mediodorsal thalamus of rats with spinal cord injury pain. *J. Neurosci.* **33**, 3915–3926 (2013).

30. Watanabe, Y. & Funahashi, S. Change of information represented by thalamic mediodorsal neurons during the delay period. *Neuroreport* **29**, 466–471 (2018).

31. Davis, M., Antoniadis, E. A., Amaral, D. G. & Winslow, J. T. Acoustic startle reflex in rhesus monkeys: a review. *Rev. Neurosci.* **19**, 171–185 (2008).

32. Zheng, A. & Schmid, S. A review of the neural basis underlying the acoustic startle response with a focus on recent developments in mammals. *Neurosci. Biobehav Rev.* **148**, 105129 (2023).

33. Dissanayake, D. W., Mason, R. & Marsden, C. A. Sensory gating, cannabinoids and schizophrenia. *Neuropharmacology* **67**, 66–77 (2013).

34. Cromwell, H. C., Mears, R. P., Wan, L. & Boutros, N. N. Sensory gating: a translational effort from basic to clinical science. *Clin. EEG Neurosci.* **39**, 69–72 (2008).

35. Jensen, O., Kaiser, J. & Lachaux, J. P. Human gamma-frequency oscillations associated with attention and memory. *Trends Neurosci.* **30**, 317–324 (2007).

36. Benchenane, K., Tiesinga, P. H. & Battaglia, F. P. Oscillations in the prefrontal cortex: a gateway to memory and attention. *Curr. Opin. Neurobiol.* **21**, 475–485 (2011).

37. Bueno-Junior, L. S., Simon, N. W., Wegener, M. A. & Moghaddam, B. Repeated Nicotine Strengthens Gamma Oscillations in the Prefrontal Cortex and Improves Visual Attention. *Neuropsychopharmacology* **42**, 1590–1598 (2017).

38. Krout, K. E., Belzer, R. E. & Loewy, A. D. Brainstem projections to midline and intralaminar thalamic nuclei of the rat. *J. Comp. Neurol.* **448**, 53–101 (2002).

39. Shin, A. et al. A brainstem-to-mediodorsal thalamic pathway mediates sound-induced arousal from slow-wave sleep. *Curr. Biol.* **33**, 875–885 e875 (2023).

40. Wong, A. B. & Borst, J. G. G. Tonotopic and non-auditory organization of the mouse dorsal inferior colliculus revealed by two-photon imaging. *Elife* **8**, https://doi.org/10.7554/eLife.49091 (2019).

41. Patel, M. B. et al. Anatomical characterization of subcortical descending projections to the inferior colliculus in mouse. *J. Comp. Neurol.* **525**, 885–900 (2017).

42. Perry, B. A. L., Lomi, E. & Mitchell, A. S. Thalamocortical interactions in cognition and disease: The mediodorsal and anterior thalamic nuclei. *Neurosci. Biobehav Rev.* **130**, 162–177 (2021).

43. James, N. M., Gritton, H. J., Kopell, N., Sen, K. & Han, X. Muscarinic receptors regulate auditory and prefrontal cortical communication during auditory processing. *Neuropharmacology* **144**, 155–171 (2019).

44. Srivastava, H. K. & Bandyopadhyay, S. Parallel Lemniscal and Non-Lemniscal Sources Control Auditory Responses in the Orbitofrontal Cortex (OFC). *eNeuro* **7**, https://doi.org/10.1523/ENEURO.0121-20.2020 (2020).

45. Panagiotaropoulos, T. I., Deco, G., Kapoor, V. & Logothetis, N. K. Neuronal discharges and gamma oscillations explicitly reflect visual consciousness in the lateral prefrontal cortex. *Neuron* **74**, 924–935 (2012).

46. Li, Z., Zhang, L., Zeng, Y., Zhao, Q. & Hu, L. Gamma-band oscillations of pain and nociception: A systematic review and meta-analysis of human and rodent studies. *Neurosci. Biobehav Rev.* **146**, 105062 (2023).

47. Ferrarelli, F. & Tononi, G. The thalamic reticular nucleus and schizophrenia. *Schizophr. Bull.* **37**, 306–315 (2011).

48. Takata, N. Thalamic reticular nucleus in the thalamocortical loop. *Neurosci. Res* **156**, 32–40 (2020).

49. Hoseini, M. S. et al. Gamma rhythms and visual information in mouse V1 specifically modulated by somatostatin(+) neurons in reticular thalamus. *Elife* **10**, https://doi.org/10.7554/eLife.61437 (2021).

50. Whitt, J. L. et al. Visual deprivation selectively reduces thalamic reticular nucleus-mediated inhibition of the auditory thalamus in adults. *J. Neurosci.* **42**, 7921–7930 (2022).

51. Jia, G., Li, X., Liu, C., He, J. & Gao, L. Stimulus-specific adaptation in auditory thalamus is modulated by the thalamic reticular nucleus. *ACS Chem. Neurosci.* **12**, 1688–1697 (2021).

52. Krause, M., Hoffmann, W. E. & Hajos, M. Auditory sensory gating in hippocampus and reticular thalamic neurons in anesthetized rats. *Biol. Psychiatry* **53**, 244–253 (2003).

Acknowledgements

Author contributions

S.W. was primarily responsible for experiment procedures and data collection; Z.L. was responsible for data analysis; B.Q., S.K. and S.F. assisted with surgical procedures and electrophysiological recording; P.Z. was responsible for experimental design; L.Q. was responsible for

experimental design, data analysis and manuscript preparation. All author contributed to and approved of the final version of the manuscript.

Competing interests

The authors declare no competing interests.

Additional information